Laser & Photonics Reviews

LASER & PHOTONICS REVIEWS

www.lpr-journal.org

RESEARCH ARTICLE OPEN ACCESS

Non-Uniform Programmable Photonic Waveguide Meshes

Cristina Catalá-Lahoz | José Capmany

Photonics Research Labs, iTEAM Research Institute, Universitat Politècnica de València, Valencia, Spain

Correspondence: Cristina Catalá-Lahoz (ccatala@iteam.upv.es)

Received: 25 September 2025 | **Revised:** 26 January 2026 | **Accepted:** 10 March 2026

Keywords: non-uniform meshes | programmable photonics | silicon photonics Vernier effect

ABSTRACT

Multipurpose photonic processors have emerged as a powerful platform for implementing diverse optical functions on a chip via software-driven reconfiguration. At the core of these processors, photonic waveguide meshes enable flexible light routing and manipulation. However, recirculating meshes are limited by the fixed dimensions of their cells, constraining their spectral and temporal resolution. Here, we introduce the concept of non-uniform programmable waveguide meshes by incorporating defect cells into a uniform hexagonal architecture. These defect cells preserve an external hexagonal perimeter while embedding smaller internal sub-cells that modify the spectral response via the Vernier effect. By coupling cells with different optical path lengths, we achieve a tenfold increase in free spectral range (FSR) up to 133 GHz and reduce sampling times from 75 to 7.5 ps, surpassing the capabilities of conventional programmable meshes. Beyond broadband signal processing, it paves the way for advanced applications in topological photonics, quantum information processing, and high-speed optical computing.

1 | Introduction

Programmable integrated photonics (PIP) [1, 2] is a new technology paradigm that aims at designing common integrated optical hardware resource configurations, capable of implementing an unconstrained variety of functionalities by suitable programming. The core of a PIP processor is a photonic waveguide mesh [3, 4], a two-dimensional lattice that provides a regular and periodic geometry, formed by replicating unit cells. The mesh connectivity determines the possible functions of the programmable circuit and how it can be configured. Broadly, waveguide meshes can be classified into forward-only [5–9], where the light flows from one side of the mesh to the other, and recirculating [10–12], where light can also be routed in loops and even back to the input ports.

Recirculating meshes typically adopt hexagonal, rectangular, or triangular geometries, where each side of the cell is formed by a tunable basic unit (TBU) composed of two integrated waveguides connected by means of a balanced Mach–Zehnder interferometer (MZI) or a gate [13–16]. The mesh is then programmed to manipulate the flow of light on a chip by electrically controlling the set of tunable analogue gates [17–19] as crossbar switches or as variable couplers with independent power division ratio and phase shift. Light is then distributed and spatially rerouted to implement various linear functions by interfering signals along different paths. PIP circuits enable broadband analogue processing, which finds applications in two relevant scenarios. The first includes applications where analogue processing is required, such as artificial intelligence [20, 21], deep learning [22], quantum information systems [23–25], and topological photonics [26, 27]. The second includes applications, such as 5 or 6G telecommunications [28], signal processing [29–31], switching and data center interconnections [32–34], hardware acceleration [35], and sensors [36], where photonic analogue processing can work in conjunction with high-speed digital electronic systems to overcome the expected limitations that arise from the death of Moore's law.

However, the performance of recirculating waveguide meshes is inherently constrained by the fixed physical dimensions of their unit cells. A typical state-of-the-art cell in silicon photonics has a side length L_s of around 450 to 900 µm, providing a propagation delay T_s in the range of 6.3 to 12.6 ps. These values are fixed once the mesh is fabricated and limit the flexibility in the spectral and time domain responses of the circuits that can be implemented. For instance, in hexagonal meshes, minimum length cavities $L = 6L_s$ provide round-trip delays between 37.6 and 75.2 ps that result in a spectral period in the range of 13.3–26.6 GHz, which is not enough for broadband applications requiring at least 40 GHz or more. Similarly, the time sampling rate achievable in the meshes is not enough for applications requiring delay precision in the range of less than 10 ps.

Here, we propose and experimentally demonstrate a solution to the above limitations that consists of embedding what we call, in analogy to solid-state physics, defect cells [37–39] into the otherwise uniform 2D hexagonal mesh. The defective cells have an external hexagonal perimeter to fit into the regular mesh, but are internally divided into sub-cells with a smaller perimeter. In this way, the individual cavities of the uniform and defect cells have slightly dissimilar spectral periods or FSR (FSR_u and FSR_d) values and the mesh spectral limitation can be solved by exploiting the Vernier effect [40, 41]. In particular, we experimentally show multiplication factors of 3.6 (FSR = 48 GHz), 6 (FSR = 80 GHz), and 10 (FSR = 133 GHz) in a hexagonal waveguide mesh implemented on a Silicon on Insulator (SOI) chip, which exceeds those achieved in a programmable photonic mesh [42]. While static microring resonators with small radii can reach FSRs exceeding 500 GHz and even approach the terahertz range, these devices lack reconfigurability and are optimized for fixed filtering applications. In addition, we show reductions of sampling times from 75 down to 7.5 ps. The foreseeable reduction of cell sidelengths to values below 100 µm, needed for scaling up programmable optical circuits [43], can open the path in combination with defect cells to the implementation of cavities offering spectral periods well beyond 1 THz and sampling times in the femtosecond range.

By inserting defect cells, it becomes possible to create non-uniform programmable waveguide meshes in which both single defects and groups of defects are deliberately placed within regular 2D layouts. The proposed modification preserves the underlying hexagonal tiling and thus retains all the advantages and functionalities of the original FPGA-like architecture. The introduction of defect cells does not compromise the hexagonal framework but enhances it by enabling novel functions while maintaining the same scalability properties without losing the inherent flexibility of the hexagonal mesh.

2 | Results

2.1 | Concept

A programmable photonic waveguide processor (Figure 1a) consists of a programmable core, optical and radiofrequency input/output interfaces, and auxiliary components that enhance performance. At the heart of this architecture lies a two-dimensional periodic waveguide mesh, typically structured in hexagonal, triangular, or square unit cells. In a hexagonal configuration, the fundamental cell perimeter, comprising six TBUs, determines the resonant cavity lengths. This inherent geometry imposes constraints on the free spectral range (FSR) and time sampling rate, limiting the processor's applicability in broadband and high-speed operations (Figure 1b).

To overcome these limitations, we propose introducing defect cells within the regular mesh, creating a non-uniform structure that enables spectral period expansion by coupling cavities of different lengths and exploiting the Vernier effect (see Note S1 for theoretical development). As an example, Figure 1c illustrates the insertion of an additional TBU to split one of the hexagonal cavities, forming a coupled system between a standard cavity with a round-trip length L and a defect cavity of length. L_d. The resulting compound cavity (Figure 1d) exhibits an extended FSR_T and a reduced time sampling rate due to the interplay between the original and defect cavity resonances.

Within the strategies for designing non-uniform meshes, we can differentiate between two types: using isolated defect cells (Figure 1e) or adding non-uniformly distributed columns (Figure 1f). In the case of isolated defect cells, specific hexagonal cavities in the mesh are individually modified by adding TBUs inside them (see Note S2). This allows the formation of compound cavities only in targeted regions of the mesh. A key advantage of this approach is that defect cells can be introduced in a localized manner, without affecting the rest of the periodic structure. On the other hand, we can create non-uniformities by adding distributed columns, modifying the length of the TBU on one side of the hexagon. These approaches can also be applied to other types of meshes, such as square meshes; however, in the latter, modifying the length of one side of a cell requires the entire row or column (depending on the mesh structure) to adopt the same length.

Leveraging the reconfigurability of the mesh, we can implement frequency-tunable ring resonators by dynamically adjusting the coupling and phase of selected MZIs. This flexibility extends to coupled cavities, where the Vernier effect allows dual tuning mechanisms: coarse and fine tuning. Coarse tuning enables a discrete frequency shift across the extended FSR by modifying the phase in one ring, whereas fine tuning provides a continuous frequency shift over a narrower bandwidth by simultaneously tuning the phase at both rings. The two approaches differ in granularity: coarse tuning operates in discrete steps determined by FSR_u or FSR_d, depending on the adjusted ring, while fine-tuning allows for precise spectral shifts down to a few GHz, depending on the resolution of the current sources used for controlling the phase actuators. By combining both tuning strategies, the entire extended FSR can be covered with high spectral precision and without additional power overhead.

2.2 | Design and Fabrication

Following the concept of non-uniform mesh with isolated defect cells, we designed and implemented a programmable hexagonal waveguide mesh comprising three distinct types of cells, as illustrated in Figure 2a. The basic cell features six tunable MZIs, each with an optical path length of L_s, resulting in a total round-trip length of $L = 6L_s$. To introduce defects, we defined two alternative cell structures. In the first case, the hexagon is

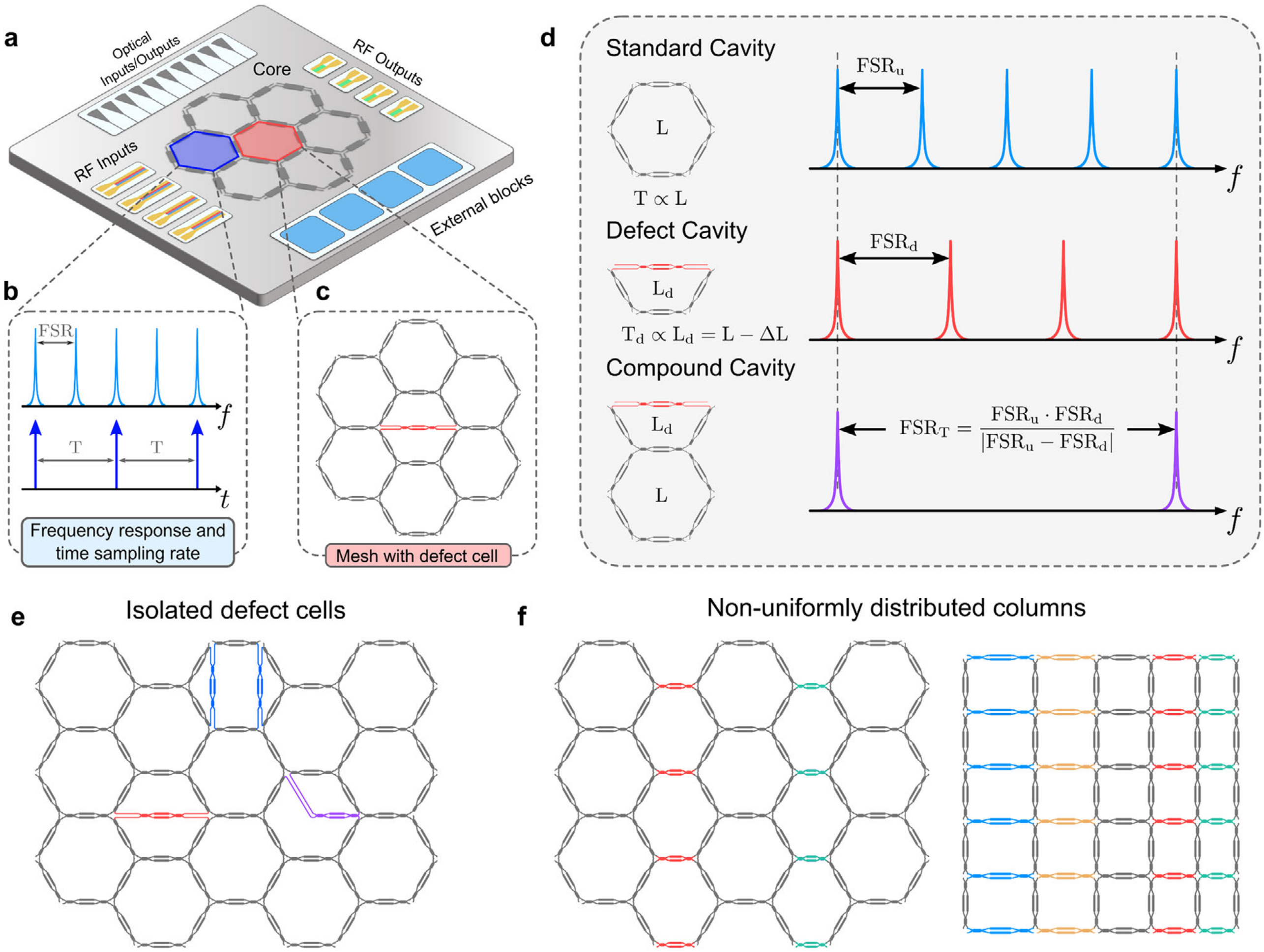

FIGURE 1 | Non-uniform programmable photonic meshes enabled by defect cells. (a) Schematic of a programmable photonic waveguide processor, comprising a reconfigurable core, optical and RF interfaces, and external control elements. (b) In conventional hexagonal meshes, cavities formed by six TBUs impose limitations on the FSR and temporal resolution. (c) A defect cell, created by introducing an additional TBU within a hexagonal cavity, alters the uniform structure, enabling new coupling mechanisms. (d) The standard and defect cavities exhibit different FSRs due to their distinct round-trip lengths (L and Ld). When combined, their spectral overlap produces an extended FSR via the Vernier effect, enhancing spectral tunability and enabling finer time resolution. (e) Concept of a non-uniform hexagonal mesh with isolated defect cells and (f) hexagonal and square meshes using non-uniformly distributed columns.

bisected into two equal defect cells, each comprising four MZIs with length L_{C1}. In the second case, the hexagon is divided asymmetrically into cells with three and five MZIs, featuring lengths L_{C2} and L_{C3}, respectively. The latter design maintains symmetry by incorporating an additional length on one side, ensuring that one MZI functions as a coupler within the ring. Importantly, both defect configurations preserve the external hexagonal perimeter, enabling seamless integration into a regular waveguide mesh.

The introduction of defect cells with varying cavity lengths facilitates an increase in the FSR through a serially coupled double-ring resonator. The FSRs of the coupled cavities must satisfy the condition $\mathrm{FS\,R_T} = m_1\ \mathrm{FS\,R_1} = m_2\ \mathrm{FSR_2}$, where m_1 and m_2 are natural, co-prime numbers [44]. By coupling cavities of lengths L_{C1} and L_{C2} we achieve FSR enhancements of 10 and 6 times, respectively, compared to the uniform hexagonal cell. Additionally, coupling L_{C2} and L_{C3} within a single hexagonal cell further increases the FSR of L_{C2} by a factor of 3, leading to an overall enhancement of 3.6 times relative to the hexagonal cavity.

Figure 2b–d illustrates circuit diagrams demonstrating these coupled double-ring resonator structures using the different cells. The transfer function at the drop port of the resulting resonator can be expressed as

$$\mathrm{H_{Drop}}(\omega) = \frac{\kappa_1\kappa_2\kappa_3\sqrt{\alpha_{R_1}\alpha_{R_2}}\,e^{j\omega\left(\frac{\tau_{R_1}+\tau_{R_2}}{2}\right)}}{1 - t_1t_2\alpha_{R_1}e^{j\omega\tau_{R_1}} - t_2t_3\alpha_{R_2}e^{j\omega\tau_{R_2}} + t_1t_3\alpha_{R_1}\alpha_{R_2}e^{j\omega\left(\tau_{R_1}+\tau_{R_2}\right)}}, \quad (1)$$

where $\kappa_{\{1,2,3\}}$ and $t_{\{1,2,3\}}$ represent the coupling and transmission coefficients of the tunable MZIs, τ_{R_1} and τ_{R_2} are the round-trip delays, ω is the optical angular frequency, and α_{R_1} and α_{R_2} These are the loss coefficients of each ring. To maximize the extinction ratio of the Vernier resonances, an optimization routine determines the optimal coupling parameters based on total ring losses.

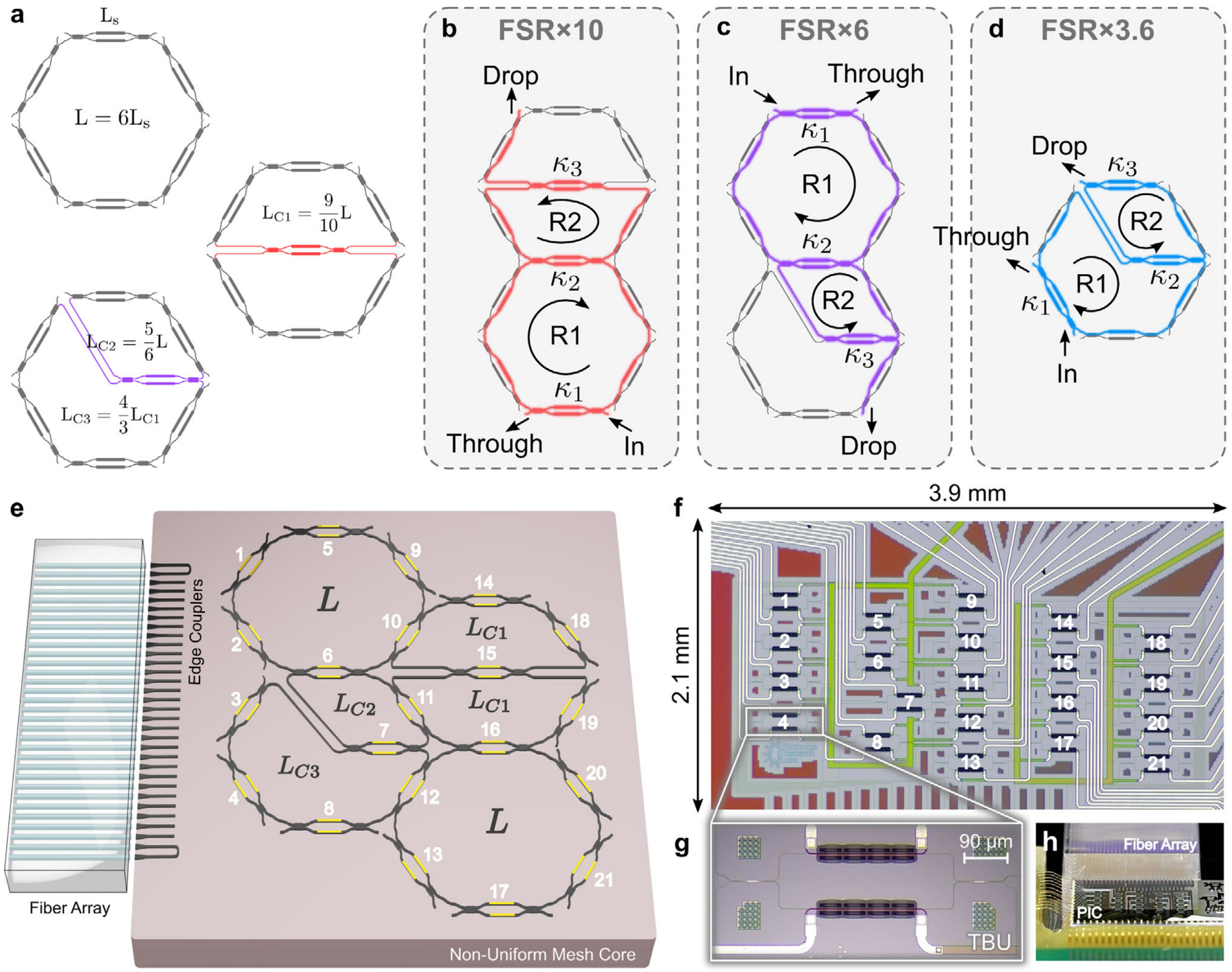

FIGURE 2 | Schematic representation of the hexagonal waveguide mesh. (a) Uniform basic cell composed of six tunable MZIs and defect cells created by splitting the hexagon into two equal parts with four MZIs each, and an asymmetric division into three and five MZI configurations. (b) Circuit diagram of coupled double-ring resonators enhancing FSR by 10 times, (c) 6 times, and (d) 3.6 times. (e) Conceptual layout of the PIC design. (f) Micrograph of the fabricated chip, showing the hexagonal waveguide mesh. (g) Low-power phase shifters utilizing suspended waveguides and trenches to minimize power consumption. (h) Packaged chip wirebonded to a PCB with fiber array alignment for optical coupling.

A non-uniform four-cell hexagonal waveguide mesh (Figure 2e) was designed and fabricated as a photonic integrated circuit (PIC) using the silicon-on-insulator (SOI) platform from Advanced Micro Foundry (see Materials and Methods). The foundry specifications include a waveguide loss of 1.1 dB/cm, multimode interferometer (MMI) insertion losses of 0.15 dB, and edge coupler insertion losses of 1.3 dB, all at a wavelength of 1550 nm.

The fabricated chip (Figure 2f) follows a flattened hexagonal mesh configuration (see Note S3 for flattened design details), in order to fit the chip size, with hexagonal sides of 900 µm for the 21 integrated MZIs. To reduce power consumption, the phase shifters employ suspended waveguides with trenches (Figure 2 g), achieving an efficiency of 1.26 mW/π and a tuning speed of ~3 kHz, which is suitable for quasi-static configurations such as programmable filters or slowly varying signal processing tasks. The chip was electrically packaged onto a printed circuit board (PCB) for precise phase control, with 24 edge couplers for optical input/output interfacing and alignment loops to facilitate fiber array alignment during coupling (Figure 2 h).

2.3 | Vernier Effect Measurements

We programmed three types of double-coupled ring resonators using the fabricated programmable mesh. To configure a photonic circuit within the mesh, we first characterized each TBU. Due to fabrication deviations, the TBUs are not perfectly balanced (see Note S3 for details on device characterization). As a result, each TBU requires different current values depending on the desired coupling, which can be programmed via software using multichannel current sources.

From a signal propagation control perspective, the introduction of defect cells does not increase algorithmic complexity. Since our routing algorithms rely on graph-based abstractions, a defect cell is treated as a node with modified attribute weights, allowing standard pathfinding algorithms (e.g., Dijkstra) to operate without modification. Regarding hardware scaling, the overhead in terms of extra phase shifters and physical control pads is minimal and linear. The total number of phase shifters (see Note S2) is given by $N_{\text{ps}} = (6\,N_h N_v + 4N_h + 4N_v - 2) + 2N_{defects}$, where N_v

TABLE 1 | Parameters of the Vernier cavities.

	FSR × 3.6			FSR × 6			FSR × 10		
Parameter	Ring 1	Ring 2	Vernier	Ring 1	Ring 2	Vernier	Ring 1	Ring 2	Vernier
L (mm)	6	4.5		5.4	4.5		5.4	4.86	
α	0.8639	0.9112		0.8478	0.9112		0.8478	0.8892	
κ_1, κ_3			0.3285			0.3714			0.2282
κ_2			0.1122			0.1530			0.1428
P_T [a] (mW)			7.45			8.92			10.15
FSR (GHz)	11.96	15.95	47.84	13.29	15.95	79.74	13.29	14.76	132.9
T (ps)	83.61	62.69	20.90	75.24	62.69	12.54	75.24	67.75	7.52
φ_{CT} (rad)	0.28π	0	0.67π	0.2π	0	0.4π	0.28π	0	0.22π
φ_{FT} (rad)	0.28π	0.28π	$0.133\ \pi$	0.28π	0.28π	0.08π	0.28π	0.28π	0.002π

The total phase shift φ is calculated on the total FSR resulting from the Vernier effect. CT: coarse tuning, FT: fine tuning.
[a]Total power consumption of the circuit.

and N_h are the number of vertical and horizontal hexagonal cells, and $N_{defects}$ is the number of inserted defect TBUs. This negligible increase (2 actuators per defect) does not compromise the mesh connectivity when using the mesh for other applications, rather than Vernier ring resonators (see Note S2 for a routing analysis of another circuit in a non-uniform mesh).

For optical measurements, we used a tunable laser combined with a component tester to characterize the ring responses (see Note S5 for setup details). The total losses per MZI are approximately 0.48 dB, implying a loss factor of $\alpha = 0.85$ for a ring formed with a hexagonal cell. Consequently, the Vernier effect response deviates from the ideal case, where the secondary to main resonance ratio will be inversely proportional to the losses.

We compared the measured amplitude and phase responses with simulated results using the response given by Equation (1), using the coupling and loss parameters specified in Table 1. Figure 3 shows the amplitude responses for the three coupled cavity cases, where experimental measurements align closely with the simulated results. Coupling the L_{C2} and L_{C3} cavities (Figure 3a) extended the FSR by a factor of 3.6 compared to a hexagonal cavity (see Supplementary Materials for individual ring measurements), yielding an FSR of 47.8 GHz. Similarly, coupling a hexagonal cavity with the L_{C3} cavity increased the FSR by a factor of six, reaching 79.7 GHz (Figure 3b). Finally, coupling a hexagonal cavity with L_{C1} yielded a tenfold FSR increase, resulting in 132.9 GHz (Figure 3c). Figure 3d–f illustrates the corresponding phase responses, derived from the Kramers-Kronig relations (see Note S6 for details), demonstrating the interaction between the resonances of both cavities. The primary resonance exhibits a 2π phase shift, while the secondary resonances show a smaller, more gradual phase variation.

Each TBU within the programmable mesh consists of an MZI with two phase shifters, one per arm, enabling precise control of coupling and phase at the output. In applications requiring only coupling adjustments, driving a single-phase shifter is enough. However, for independent control of both coupling and phase, both phase shifters must be modulated (Figure 4a). The coupling constant is given by $\kappa = \cos^2\left(\frac{\phi_2-\phi_1}{2}\right)$, while the overall phase shift follows $\varphi = (\phi_1 + \phi_2)/2$.

Figure 4 shows the measurements of the different Vernier cavities being shifted throughout the entire FSR using fine and coarse tuning techniques in all cases. The reference column illustrates the spectral response of each circuit extended over multiple spectral periods, and their response can be tuned in two ways. Fine-tuning is performed by operating one of the MZIs in each ring as a phase shifter, applying the same current difference to both rings (Figure 4b). In our experiments, we adjusted the response in 3.2 GHz steps, corresponding to a power difference of $\Delta P = 0.35$ mW per phase shifter. The maximum frequency shift is limited by the breakdown current or voltage of the phase shifter (8.39 mA), and the minimum is determined by the resolution of the current sources.

Coarse spectral tuning is achieved by applying a phase shift to only one ring (Figure 4c), altering its resonance while leaving the second ring fixed, thus adjusting the Vernier effect to match the next resonance of the second cavity. In Figure 4d,e coarse tuning was performed by shifting the response of the L_{C3} and the hexagonal ring, respectively, achieving a 15.95 GHz frequency step in both cases, resulting from the non-tuned ring L_{C2}. For the circuit in Figure 4f, coarse tuning of the hexagonal ring resulted in a 14.76 GHz frequency step, enabling tuning across the entire FSR of 132.9 GHz. Two different tuning steps are possible when doing coarse tuning, depending on the ring you shift. In this configuration, you will obtain a tuning step equal to the FSR of the non-tuned ring. By combining fine and coarse tuning, we can continuously shift the response of these rings over the extended FSR, making the system highly reconfigurable in frequency. Table 1 lists the coupling parameters and current values used for each case, including those for both fine and coarse tuning.

Additionally, inserting defective cells allows for a reduction in sampling time resolution, addressing the limitation found in uniform waveguide meshes. To demonstrate this, we measured

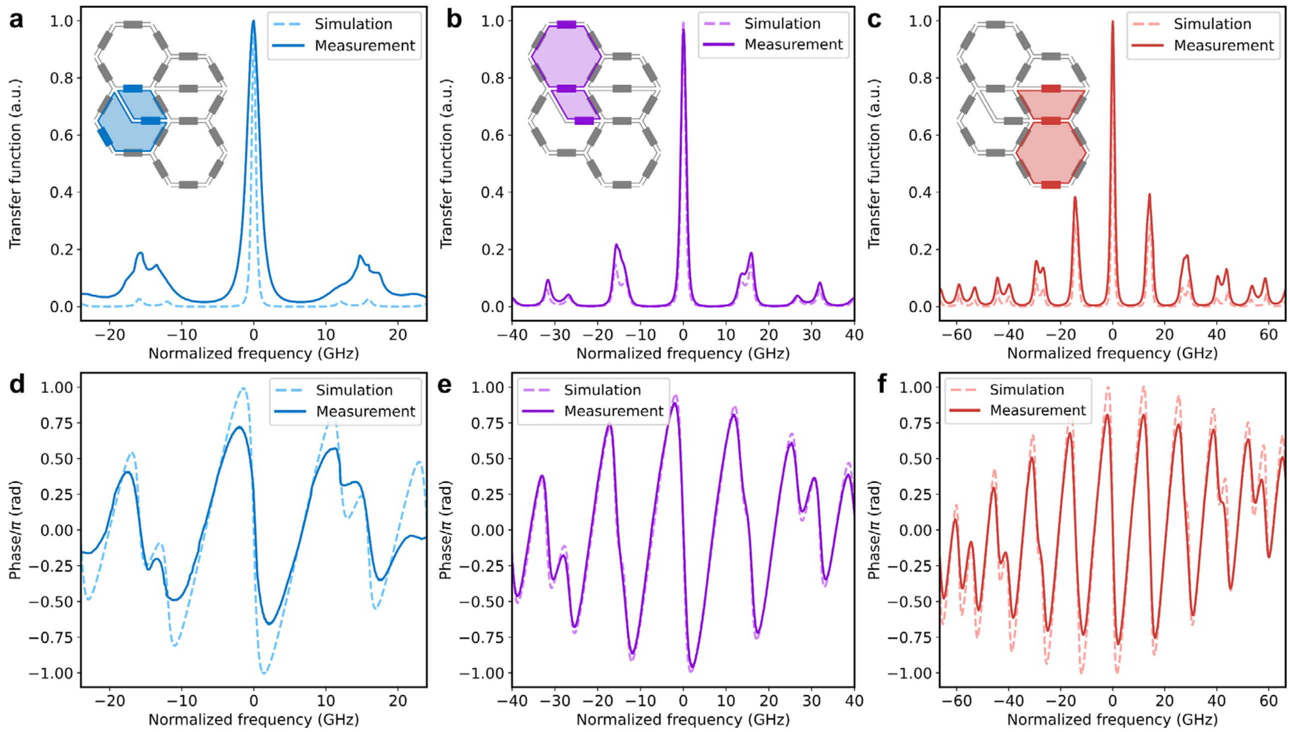

FIGURE 3 | Comparison between simulation and experimental measurements of the three Vernier cavities. (a–c) Measured amplitude response for the three coupled cavity configurations. Experimental results (solid lines) are compared with the simulated response (dashed lines). The coupling and loss parameters used in the simulations are listed in Table 1. (d–f) Corresponding phase response, derived using Kramers–Kronig relations, showing the interaction between the resonances of the two cavities. The primary resonance exhibits a 2π phase shift, while secondary resonances show a smaller phase variation.

the temporal response of each cavity within the mesh using 1-picosecond Gaussian pulses. Figure 5a–d shows the sampling time between consecutive pulses for each independent cavity, achieving resolutions ranging from 62.69 to 83.61 ps. Using the Vernier effect, we further reduced the resolution. Figure 5e–g illustrates the temporal responses of the coupled cavities with different lengths, achieving sampling times as low as 7.52 to 20.9 ps. This reduction is especially beneficial for applications requiring extremely high delay precision.

3 | Discussion

In this work, we have proposed, fabricated, and experimentally demonstrated a non-uniform programmable photonic mesh in silicon on insulator. Specifically, we introduced defects within a hexagonal mesh structure to break the uniformity of the cavities and path length sections. By coupling two or more cavities with different round-trip lengths, we successfully implemented filters with an extended FSR, leveraging the Vernier effect to enhance performance. This approach addresses a critical limitation in uniform programmable hexagonal meshes, where each cavity comprises six MZIs, leading to long ring resonators with inherently small FSRs.

One question of interest is related to the effect that inserting defect cells can have on the structural redundancy offered by uniform meshes. This feature is quite important as this redundancy underpins their reconfigurability and universality by allowing the implementation of multiple circuits, and equally important, because it enables the self-healing of implemented circuits in the event that one or several TBUs fail. The defect cells proposed in this work show a key feature; they all have an external hexagonal perimeter, so the mesh structural redundancy is not affected by their inclusion if defect cells are placed in the external perimeter of the mesh. If the cells are inserted in the interior region and they cannot be used to implement a given circuit, they can always be circumvented by setting their TBUs to the bar state.

To validate our concept, we designed and fabricated a compact proof-of-concept device featuring four hexagonal cavities, two of which incorporate an internal MZI that splits the cavity. Using this programmable mesh, we demonstrated three different coupled-cavity filters with extended FSRs, achieving ring resonator responses with FSR values of 47.8, 79.7, and 132.9 GHz. In contrast, a uniform mesh of the same fabricated size yields a maximum FSR of only 13.3 GHz, indicating a tenfold improvement. Furthermore, our approach enables a significantly reduced time sampling rate, which is crucial for high-speed optical signal processing. We obtained time sampling values of 20.9, 12.5, and 7.5 ps using the Vernier cavities, compared to approximately 75 ps when utilizing a single hexagonal cavity.

This study paves the way for further advancements in non-uniform programmable photonic meshes. A promising direction is scalability, where larger meshes incorporating multiple defect cells could be designed to achieve even higher FSR multiplication factors, reducing the size of the TBU and improving

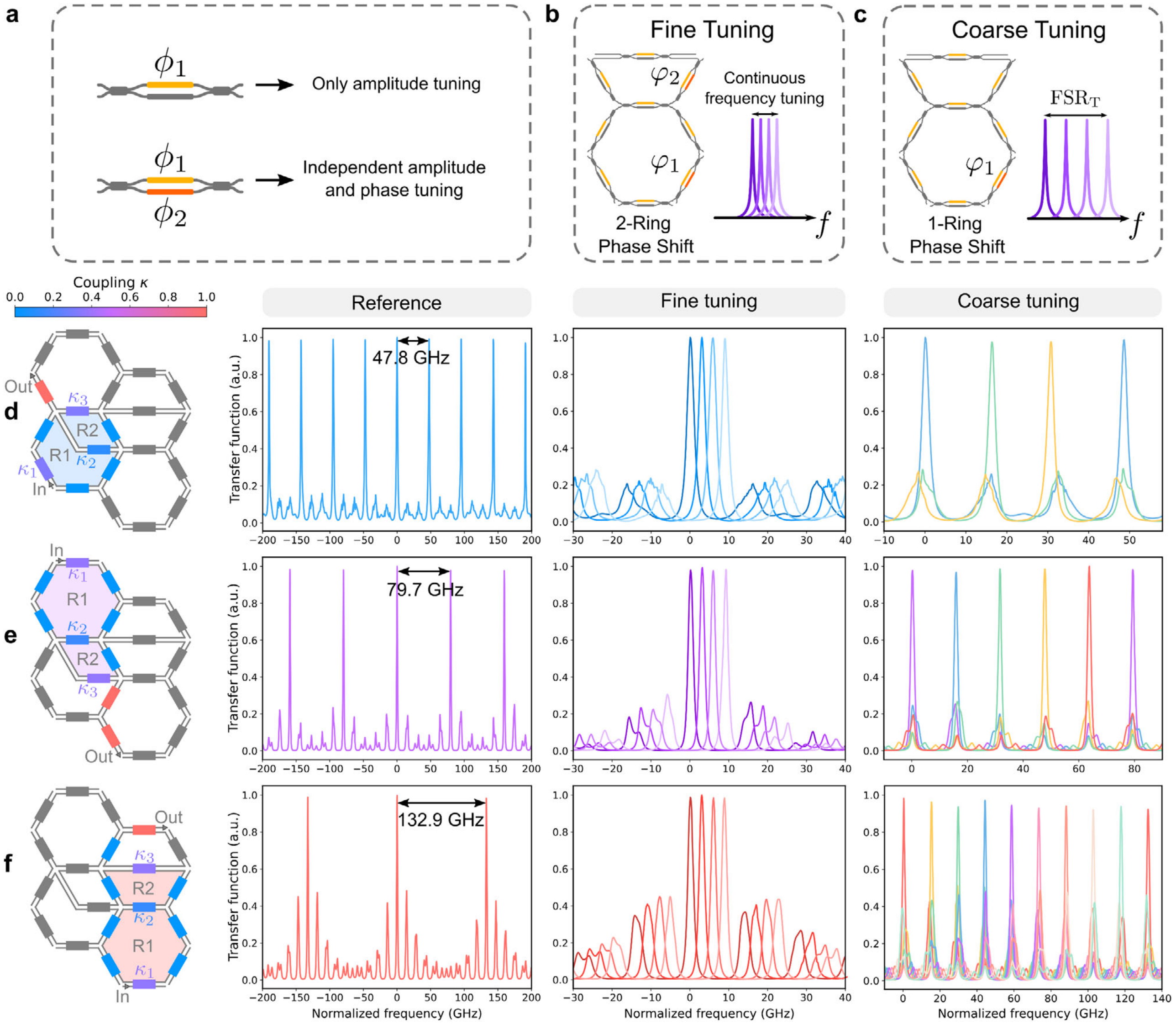

FIGURE 4 | Fine and coarse tuning measurements of the three different programmable Vernier cavities. (a) Driving one phase shifter of an MZI allows only amplitude tuning, and driving both phase shifters allows independent tuning of amplitude and phase at the output. (b) Fine tuning of the response needs shifting the response of the two rings simultaneously and (c) coarse tuning needs shifting only one ring. (d) Coupling $\mathbf{L_{C2}}$ and $\mathbf{L_{C3}}$ results in a 3.6 × FSR extension to 47.8 GHz. (e) Coupling a hexagonal cavity with $\mathbf{L_{C3}}$ results in a 6 × FSR increase, reaching 79.7 GHz. (f) Coupling a hexagonal cavity with $\mathbf{L_{C1}}$ results in a 10 × FSR increase, yielding 132.9 GHz.

overall system efficiency. The reported 0.48 dB loss per MZI is a limiting factor affecting side resonance suppression in the observed Vernier spectrum. While this loss level is comparable to other implementations of silicon photonic meshes [17, 45], it underscores the need for further optimization. For example, by reducing this value to 0.1 dB/TBU, the hexagonal mesh can be scaled up to 50 cells, resulting in a total mesh loss of 5 dB [1]. Emerging solutions such as Phase Change Materials (PCM) and Micro-Electro-Mechanical Systems (MEMS) offer some advantages [46, 47], although they may involve trade-offs in terms of tuning speed, resolution, power consumption, or fabrication complexity.

Although high-Q single and multi-ring resonators can deliver excellent performance in terms of resonance sharpness and compactness, they remain inherently limited to specific functionalities and require careful tailoring for each application. By contrast, the defect-modified hexagonal mesh architecture is designed as a universal, reconfigurable platform, where a single layout can be programmed to implement a wide range of circuits without redesign. The aim of this work is therefore not to compete with specialized devices, but to establish the mesh as the foundational approach for truly general-purpose photonic integration. A critical advantage of embedding Vernier elements within the mesh, as opposed to using external standalone resonators, is the preservation of resources. First, regarding port efficiency, a standalone high-performance ring requires dedicated input and output access. Connecting a signal from the mesh to such an external block and back would consume external optical ports of the processor. Second, regarding insertion loss, routing a signal out of the mesh to an external circuit and re-coupling it back introduces significant additional propagation loss depending on the interconnect length required to reach the external block. By embedding the defect inside the mesh, we process the signal

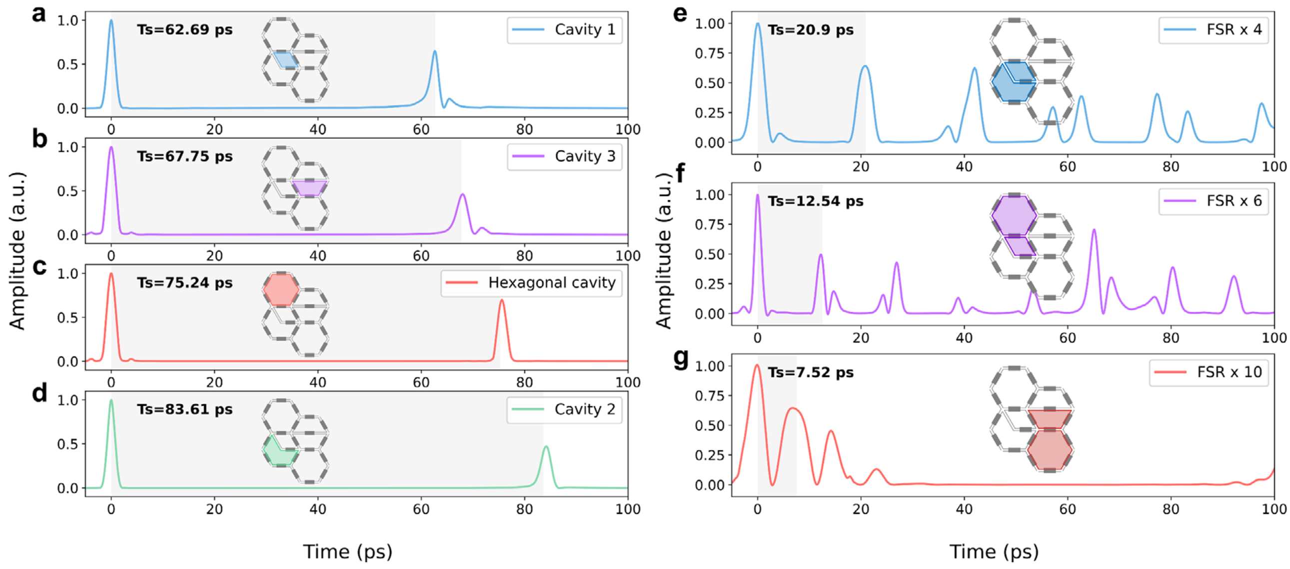

FIGURE 5 | Temporal responses using 1-picosecond Gaussian pulses. (a–d) Responses for each independent cavity, with resolutions ranging from 62.69 to 83.61 ps. (e–g) Temporal responses of the coupled cavities of different lengths, demonstrating a significant reduction in sampling times to a range of 7.5 to 20.9 ps. This improvement is particularly useful for applications requiring precise delay measurements.

in situ, maximizing link budget efficiency and saving TBUs compared to the overhead of interconnecting external building blocks.

The realization of a widely tunable and extended FSR is critical for specific application domains. In Microwave Photonics, periodic spectral resonances can interfere with wideband RF signals (e.g., in 5G/6G systems) [28]. By extending the FSR to 133 GHz, we clear a wider spectral window for processing high-frequency signals without aliasing. Additionally, in elastic optical networks, the ability to dynamically tune the filtering bandwidth and FSR allows the processor to act as a flexible bandwidth variable filter, adapting to different channel grids or routing varied wavelength division multiplexing signals without hardware replacement [48]. The reduced sampling interval brings advantages in optical beam-forming networks and arbitrary waveform generation [49, 50]. In phased array antennas, the precision of the beam steering angle depends on the minimum delay step achievable. By reducing the sampling unit to ~7.5 ps via defect cells, our architecture enables high-resolution true time delay lines, satisfying the requirements of modern radar and satellite communications. For AWG applications, it opens the door to the generation of reconfigurable pulse shaping at different carrier frequencies (in our particular example shown here at 12, 13.3, 14.8, 16, 48, 80, and 133,4 GHz) [51].

Beyond classical applications, non-uniform photonic meshes provide a highly adaptable platform for emerging fields such as topological photonic devices [12], the implementation of physically unclonable functions (PUFs) [52], and quantum photonics [53], offering new opportunities for advanced photonic computing and signal processing architectures. However, while quantum information processing is a promising direction, it imposes much stricter performance requirements. In particular, optical losses would need to be significantly reduced (down to approximately 0.01 dB per TBU), which would require substantial additional engineering efforts.

The current TBU design of this work has a length of 900 μm, as we used the process design kit (PDK) phase shifters and MMIs from the foundry. A custom design could reduce the TBU size to approximately 100 μm, enabling operation bandwidths of around 120 GHz for hexagonal cavities and up to 1.2 THz for the proposed non-uniform mesh, but sacrificing some power consumption [54, 55]. Additionally, minimizing TBU losses will further enhance the performance of the Vernier effect, leading to higher extinction ratios in the main resonances. The current loss of approximately 0.48 dB per TBU could potentially be reduced to around 0.08 dB [56], enabling applications in ultra-broadband optical processing and high-speed optical communications.

4 | Materials and Methods

4.1 | Fabrication of the Device

The photonic integrated circuit was fabricated by Advanced Micro Foundry using a standard silicon on insulator process. The chip was produced from an SOI wafer with a 220 nm device layer, featuring 500 nm single-mode waveguides patterned through deep ultraviolet (193 nm) lithography. Phase-shifting waveguide sections were implemented by depositing a 120 nm TiN heater layer over the waveguides, powered by 2000 nm-thick metal DC tracks added in the final stages of fabrication. The process allows the doping of waveguides and under-etched waveguides to improve the efficiency of the phase actuators and mitigate thermal crosstalk effects. The chip size is $2.8 \times 4.3\ mm^2$, including electrical pads and edge couplers.

4.2 | Device Characterization and Measurements

Manufacturing deviations affect the optical phase of the elements that compound the programmable mesh. Characterization of all the MZIs is needed to correctly drive the currents at each thermal tuner. This process was performed using a continuous wave laser fixed at 1550 nm and a power meter (FTBx-1750 EXFO) to measure the output optical power while driving the phase shifters. The 42 DC channels are wirebonded to a printed circuit board (PCB) and controlled with a multichannel current source (Qontrol Ltd.) that can be programmed through coding. A more detailed explanation of the calibration process can be found in Note S4. After calibration, each TBU has its own set of current values for a certain coupling and phase.

For optical spectral measurements, we used a tunable laser source (T100S-HP EXFO) along with a component tester (CT440 EXFO), featuring a 1 pm wavelength resolution. Active optical alignment was performed automatically using piezo controllers (Thorlabs MDT693B) for the positioner that held the fiber array. The alignment routine consists of finding, simultaneously, high optical output power at both loops of the edge coupler array. A 7 dB loss is measured for the loop ports, corresponding to a 3.5 dB loss per input, including the coupling and insertion losses of the edge couplers.

To have a stable temperature during measurements, we use a temperature controller (Thorlabs TED200C) along with a Peltier cooler and a thermistor, setting a chip temperature around 25°C. A heatsink was placed under the whole packaged device for heat dissipation.

Acknowledgements

The authors acknowledge the financial support of the European Research Council (ERC) under Grant Agreement Nos. 101138302 (NU-MESH) and 101097092 (ANBIT). This work was also supported by the COMCUANTICA/005 and COMCUANTICA/006 grants, which are funded by the European Union through NextGenerationEU (PRTR-C17), the Spanish Ministry of Science and Innovation, and the Generalitat Valenciana. Finally, we acknowledge funding from the Generalitat Valenciana through the PROMETEO/2021/015 project.

Conflicts of Interest

The authors declare no conflicts of interest.

Data Availability Statement

The data that support the findings of this study are available from the corresponding authors upon reasonable request.

References

1. J. Capmany and D. Pérez, *Programmable Integrated Photonics* (Oxford University Press, 2020), https://doi.org/10.1093/oso/9780198844402.001.0001.

2. W. Bogaerts, D. Pérez, J. Capmany, et al., "Programmable Photonic Circuits," *Nature* 586 (2020): 207–216, https://doi.org/10.1038/s41586-020-2764-0.

3. L. Zhuang, C. G. H. Roeloffzen, M. Hoekman, K. J. Boller, and A. J. Lowery, "Programmable Photonic Signal Processor Chip for Radiofrequency Applications," *Optica* 2 (2015): 854–859, https://doi.org/10.1364/OPTICA.2.000854.

4. D. Pérez, I. Gasulla, J. Capmany, and R. A. Soref, "Reconfigurable Lattice Mesh Designs for Programmable Photonic Processors," *Optics Express* 24 (2016): 12093–12106.

5. N. C. Harris, J. Carolan, D. Bunandar, et al., "Linear Programmable Nanophotonic Processors," *Optica* 5 (2018): 1623–1631, https://doi.org/10.1364/OPTICA.5.001623.

6. D. A. B. Miller, "Self-Configuring Universal Linear Optical Component [Invited]," *Photonics Research* 1 (2013): 1–15, https://doi.org/10.1364/PRJ.1.000001.

7. W. R. Clements, P. C. Humphreys, B. J. Metcalf, W. S. Kolthammer, and I. A. Walmsley, "Optimal Design for Universal Multiport Interferometers," *Optica* 3 (2016): 1460–1465, https://doi.org/10.1364/OPTICA.3.001460.

8. M. Reck, A. Zeilinger, H. J. Bernstein, and P. Bertani, "Experimental Realization of any Discrete Unitary Operator," *Physical Review Letters* 73 (1994): 58–61, https://doi.org/10.1103/PhysRevLett.73.58.

9. A. Ribeiro, A. Ruocco, L. Vanacker, and W. Bogaerts, "Demonstration of a 4 × 4-Port Universal Linear Circuit," *Optica* 3 (2016): 1348–1357, https://doi.org/10.1364/OPTICA.3.001348.

10. D. Pérez, I. Gasulla, and J. Capmany, "Multipurpose Silicon Photonics Signal Processor Core," *Nature Communications* 8 (2017): 636.

11. D. Pérez-López, A. M. Gutierrez, E. Sánchez, P. DasMahapatra, and J. Capmany, "Integrated Photonic Tunable Basic Units Using Dual-Drive Directional Couplers," *Optics Express* 27 (2019): 38071–38086.

12. T. Dai, A. Ma, J. Mao, et al., "A Programmable Topological Photonic Chip," *Nature Materials* 23 (2024): 928–936, https://doi.org/10.1038/s41563-024-01904-1.

13. D. A. B. Miller, "Perfect Optics with Imperfect Components," *Optica* 2 (2015): 747–750, https://doi.org/10.1364/OPTICA.2.000747.

14. M. Wang, A. Ribero, Y. Xing, and W. Bogaerts, "Tolerant, Broadband Tunable 2 × 2 Coupler Circuit," *Optics Express* 28 (2020): 5555–5566, https://doi.org/10.1364/OE.384018.

15. D. Pérez, I. Gasulla, and J. Capmany, "Field-Programmable Photonic Arrays," *Optics Express* 26 (2018): 27265–27278.

16. A. Rahim, T. Spuesens, R. Baets, and W. Bogaerts, "Open-access Silicon Photonics: Current Status and Emerging Initiatives," *Proceedings of the IEEE* 106 (2018): 2313–2330, https://doi.org/10.1109/JPROC.2018.2878686.

17. D. Pérez-López, A. López, P. DasMahapatra, and J. Capmany, "Multipurpose Self-Configuration of Programmable Photonic Circuits," *Nature Communications* 11 (2020): 636.

18. Z. Gao, X. Chen, Z. Zhang, U. Chakraborty, W. Bogaerts, and D. S. Boning, "Gradient-Based Power Efficient Functional Synthesis for Programmable Photonic Circuits," *Journal of Lightwave Technology* 42 (2024): 5956–5965, https://doi.org/10.1109/JLT.2024.3400942.

19. D. A. B. Miller, "Self-Configuring Programmable Photonics for Processing, Communications and Sensing," in Optical Fiber Communication Conference (OFC), (IEEE, 2022), https://doi.org/10.1364/OFC.2022.M2G.1.

20. A. N. Tait, M. A. Nahmias, B. J. Shastri, and P. R. Prucnal, "Broadcast and Weight: an Integrated Network for Scalable Photonic Spike Processing," *Journal of Lightwave Technology* 32 (2014): 4029–4041, https://doi.org/10.1109/JLT.2014.2345652.

21. B. J. Shastri, A. N. Tait, T. Ferreira De Lima, et al., "Photonics for Artificial Intelligence and Neuromorphic Computing," *Nature Photonics* 15 (2021): 102–114, https://doi.org/10.1038/s41566-020-00754-y.

22. Y. Shen, N. C. Harris, S. Skirlo, et al., "Deep Learning with Coherent Nanophotonic Circuits," *Nature Photonics* 11 (2017): 441–446, https://doi.org/10.1038/nphoton.2017.93.

23. J. Carolan, C. Harrold, C. Sparrow, et al., "Universal Linear Optics," *Science* 349 (2015): 711–716, https://doi.org/10.1126/science.aab3642.

24. N. C. Harris, G. R. Steinbrecher, M. Prabhu, et al., "Quantum Transport Simulations in a Programmable Nanophotonic Processor," *Nature Photonics* 11 (2017): 447–452, https://doi.org/10.1038/nphoton.2017.95.

25. J. Wang, S. Paesani, Y. Ding, et al., "Multidimensional Quantum Entanglement with Large-Scale Integrated Optics," *Science* 360 (2018): 285–291, https://doi.org/10.1126/science.aar7053.

26. M. B. On, D. Pérez-López, P. DasMahapatra, and J. Capmany, "Programmable Integrated Photonics for Topological Hamiltonians," *Nature Communications* 15 (2024): 629, https://doi.org/10.1038/s41467-024-44939-3.

27. J. Capmany and D. Pérez-López, "Programming Topological Photonics," *Nature Materials* 23 (2024): 874–875, https://doi.org/10.1038/s41563-024-01932-x.

28. D. Pérez-López, A. Gutierrez, D. Sánchez, et al., "General-Purpose Programmable Photonic Processor for Advanced Radiofrequency Applications," *Nature Communications* 15 (2024): 1563.

29. S. Hong, J. Wu, Y. Xie, et al., "Versatile Parallel Signal Processing with a Scalable Silicon Photonic Chip," *Nature Communications* 16 (2025): 288, https://doi.org/10.1038/s41467-024-55162-5.

30. X. Zhou, D. Yi, D. W. U. Chan, and H. K. Tsang, "Silicon Photonics for High-Speed Communications and Photonic Signal Processing," *npj Nanophotonics* 1 (2024): 27, https://doi.org/10.1038/s44310-024-00024-7.

31. A. N. Amiri, A. D. Vit, K. Gorgulu, and E. S. Magden, "Deep Photonic Network Platform Enabling Arbitrary and Broadband Optical Functionality," *Nature Communications* 15 (2024): 1432, https://doi.org/10.1038/s41467-024-45846-3.

32. N. Quack, H. Sattari, A. Y. Takabayashi, et al., "MEMS-Enabled Silicon Photonic Integrated Devices and Circuits," *IEEE Journal of Quantum Electronics* 56 (2020): 1–10, https://doi.org/10.1109/JQE.2019.2946841.

33. Y. Hu, Y. Sun, Y. Lu, et al., "Silicon Photonic MEMS Switches Based on Split Waveguide Crossings," *Nature Communications* 16 (2025): 331, https://doi.org/10.1038/s41467-024-55528-9.

34. Y. Ding, V. Kamchevska, K. Dalgaard, et al., "Reconfigurable SDM Switching Using Novel Silicon Photonic Integrated Circuit," *Scientific Reports* 6 (2016): 39058, https://doi.org/10.1038/srep39058.

35. J. Feldmann, N. Youngblood, C. D. Wright, H. Bhaskaran, and W. H. P. Pernice, "Parallel Convolutional Processing Using an Integrated Photonic Tensor Core," *Nature* 589 (2021): 52–58, https://doi.org/10.1038/s41586-020-03070-1.

36. T. Hu, B. Dong, X. Luo, et al., "Silicon Photonic Platforms for Mid-infrared Applications [Invited]," *Photonics Research* 5 (2017): 417–430, https://doi.org/10.1364/PRJ.5.000417.

37. N. Ashcroft and N. Mermin, *Solid State Physics* (Cengage Learning, 2003).

38. E. Yablonovitch, "Inhibited Spontaneous Emission in Solid-State Physics and Electronics," *Physical Review Letters* 58 (1987): 2059–2062, https://doi.org/10.1103/PhysRevLett.58.2059.

39. S. John, "Strong Localization of Photons in Certain Disordered Dielectric Superlattices," *Physical Review Letters* 58 (1987): 2486–2489, https://doi.org/10.1103/PhysRevLett.58.2486.

40. W. Bogaerts, P. De Heyn, T. Van Vaerenbergh, et al., "Silicon Microring Resonators," *Laser & Photonics Reviews* 6 (2012): 47–73, https://doi.org/10.1002/lpor.201100017.

41. J. C. Hulme, J. K. Doylend, and J. E. Bowers, "Widely Tunable Vernier Ring Laser on Hybrid Silicon," *Optics Express* 21 (2013): 19718–19722, https://doi.org/10.1364/OE.21.019718.

42. L. Zhuang, M. Hoekman, W. Beeker, et al., "Novel Low-Loss Waveguide Delay Lines Using Vernier Ring Resonators for on-Chip Multi-λ Microwave Photonic Signal Processors," *Laser & Photonics Reviews* 7 (2013): 994–1002, https://doi.org/10.1002/lpor.201300053.

43. W. Bogaerts and G. T. Reed, "Scaling Programmable Silicon Photonics Circuits," in *Silicon Photonics XVIII*, ed. G. T. Reed and A. P. Knights (SPIE, 2023), 1242601, https://doi.org/10.1117/12.2647293.

44. D. Rabus, "Integrated Ring Resonators: the Compendium," *Springer Series in Optical Sciences* (Springer, 2007).

45. Y. Zhang, "A Compact Programmable Silicon Photonic Circuit," in *IEEE Silicon Photonics Conference (SiPhotonics)*, (IEEE, 2024), 1–2.

46. J. Xia, T. Wang, Z. Wang, et al., "Seven Bit Nonvolatile Electrically Programmable Photonics Based on Phase-change Materials for Image Recognition," *ACS Photonics* 11 (2024): 723–730, https://doi.org/10.1021/acsphotonics.3c01598.

47. M. Dong, J. M. Boyle, K. J. Palm, et al., "Synchronous Micromechanically Resonant Programmable Photonic Circuits," *Nature Communications* 14 (2023): 7716, https://doi.org/10.1038/s41467-023-42866-3.

48. S. Zhu, B. Yuan, Y. Fan, et al., "A Reconfigurable Multi-Channel on-Chip Photonic Filter for Programmable Optical Frequency Division," *Nanophotonics* 14 (2025): 2619, https://doi.org/10.1515/nanoph-2025-0119.

49. P. Martinez-Carrasco, T. H. Ho, D. Wessel, and J. Capmany, "Ultrabroadband High-Resolution Silicon RF-photonic Beamformer," *Nature Communications* 15 (2024): 1433, https://doi.org/10.1038/s41467-024-45743-9.

50. J. Wang, H. Shen, L. Fan, et al., "Reconfigurable Radio-Frequency Arbitrary Waveforms Synthesized in a Silicon Photonic Chip," *Nature Communications* 6 (2015): 5957, https://doi.org/10.1038/ncomms6957.

51. L. M. Cohen, K. Wu, K. V. Myilswamy, S. Fatema, N. B. Lingaraju, and A. M. Weiner, "Silicon Photonic Microresonator-based High-Resolution Line-By-Line Pulse Shaping," *Nature Communications* 15 (2024): 7878, https://doi.org/10.1038/s41467-024-52051-9.

52. A. M. Smith and H. S. Jacinto, "Reconfigurable Integrated Optical Interferometer Network-Based Physically Unclonable Function," *Journal of Lightwave Technology* 38 (2020): 4599–4606, https://doi.org/10.1109/JLT.2020.2996015.

53. M. Dong, D. Pérez-López, and J. Capmany, "Programmable Photonic Integrated Meshes for Modular Generation of Optical Entanglement Links," *npj Quantum Information* 9 (2023): 42, https://doi.org/10.1038/s41534-023-00708-6.

54. Y. Liu, Z. Li, S. Wang, et al., "Ultra-Compact and Polarization-Insensitive MMI Coupler Based on Inverse Design," in *Optical Fiber Communications Conference and Exhibition (OFC)*, (IEEE, 2019), 1–3.

55. N. C. Harris, Y. Ma, J. Mower, et al., "Efficient, Compact and Low Loss Thermo-Optic Phase Shifter in Silicon," *Optics Express* 22 (2014): 10487–10493, https://doi.org/10.1364/OE.22.010487.

56. N. C. Harris, "Passage: a Wafer-Scale Programmable Photonic Communication Substrate," in *IEEE Hot Chips 34 Symposium (HCS)*, (IEEE, 2022), 1–26, https://doi.org/10.1109/HCS55958.2022.9895610.

Supporting Information

Additional supporting information can be found online in the Supporting Information section.

Supporting File: lpor71114-sup-0001-SuppMat.docx.